Int. J. Heat Mass Transfer. Vol. 36, No. 5, pp. 1201–1218, 1993
Printed in Great Britain

0017-9310/93 $6.00 + 0.00
Pergamon Press Ltd

Computations of liquid immersion cooling for a protruding heat source in a cubical enclosure

DONALD E. WROBLEWSKI† and YOGENDRA JOSHI
Naval Postgraduate School, Monterey, CA 93943, U.S.A.

(*Received* 20 *September* 1991 *and in final form* 5 *June* 1992)

Abstract—Three-dimensional natural convection flow and heat transfer were studied numerically for a heated, protruding substrate-mounted chip or package in a cubic enclosure filled with a dielectric liquid. The governing steady-state equations for the natural convection within the liquid and the conjugate conduction within the element and the substrate were solved using a finite-volume method over a wide range of Rayleigh numbers (Ra) and substrate-to-fluid thermal conductivity ratios (R_s). Conduction through the substrate plays a dominant role in the cooling of the chip for values of R_s greater than 10. Comparison of the numerical results with experimental data showed reasonable agreement, particularly in the patterns of isotherms observed on the substrate surface.

1. INTRODUCTION

THERMAL control of electronic components using dielectric liquids has recently received increased attention due to inherently high heat removal capabilities of liquids compared with air. Both single phase and phase change schemes for these applications have been reviewed by Bar-Cohen [1]. Passive cooling presents an attractive option for enclosed systems such as power supplies and certain electronic modules due to its high reliability and resulting design compactness. The transport in such geometrically complex systems is often three-dimensional and includes discrete heating conditions and multiple heat transfer paths. While two-dimensional investigations have been made to examine the natural convection flow and heat transfer in liquids due to discrete heating [2–5], three-dimensional effects remain much less studied.

As seen in Table 1, previous numerical studies [6–22] of three-dimensional natural convection in rectangular enclosures can be classified into four distinct categories: (1) enclosures with bottom heated and top cooled; (2) enclosures with opposite vertical walls heated and cooled; (3) tilted enclosures with opposite walls heated and cooled; and (4) enclosures with concentrated heat sources on one wall. Most of the studies listed above [6–18] fall under the first three categories. The last group represents models of heated electronic components flush mounted on, or protruding from, one or more enclosure surfaces.

Kuhn and Oosthuizen [19] found that for a flush vertical element, the three-dimensional flow tends to increase the mean Nusselt number from the element compared with the two-dimensional calculations, mostly through increased heat transfer at the edges. However, the effect was dependent upon Rayleigh number and location of the element. Interestingly, the steady-state Nusselt number was closer to the two-dimensional result for higher Rayleigh numbers, which is opposite to the behavior observed when the entire wall is heated [13].

A 3×3 array of protruding heat sources on a vertical wall was investigated by Liu *et al.* [20, 21]. A uniform heat flux surface condition was applied to the protrusion faces. They found that there was little interference among chips and that the heat transfer was affected more by the stratified temperature field outside of the boundary layer region than by relative position within the boundary layer. Long-time solutions were characterized by temperature oscillations on the faces.

The present study examines the natural convection from a substrate mounted protrusion in a cubical enclosure. The substrate forms one vertical wall of the enclosure. The opposite vertical wall is cooled, and maintained at a constant temperature, while all other surfaces are insulated. The current work falls in the last category discussed above, although it is unique even among these studies in that the boundary conditions along the chip and substrate surfaces are not specified. Instead, a uniform volumetric heat generation is specified for the protrusion, and the conjugate conduction within the heat source and the substrate is solved in addition to the natural convection flow within the enclosure. Because the substrate is conducting heat, the problem exhibits some similarities to the case of an enclosure with opposite heated and cooled vertical walls.

The main objective of the current work is to examine the effect of Rayleigh number and substrate ther-

†Current address: Department of Aerospace and Mechanical Engineering, Boston University, Boston, MA 02215, U.S.A.

NOMENCLATURE

C	ratio of ρc_p of substrate or chip to ρc_p of fluid, $((\rho c_p)/(\rho c_p)_f)$	T_c	temperature at the cold enclosure wall parallel to the substrate [K]
c_p	specific heat at constant pressure [J kg^{-1} K^{-1}]	u	horizontal velocity component [m s^{-1}]
g	gravitational acceleration [m s^{-2}]	v	vertical velocity component [m s^{-1}]
h_c	thickness of protrusion [m]	w	spanwise velocity component [m s^{-1}]
h_s	thickness of substrate [m]	x	horizontal coordinate [m]
k	thermal conductivity [W m^{-1} K^{-1}]	y	vertical coordinate [m]
l	protrusion length [m]	z	spanwise coordinate [m].
L	enclosure length [m]	Greek symbols	
Nu	Nusselt number, $(q_i L/k_f(T_i - T_c))$	α	fluid thermal diffusivity [m^2 s^{-1}]
p	pressure [N m^{-2}]	β	coefficient of thermal expansion [K^{-1}]
Pr	Prandtl number of fluid, (ν/α)	ν	kinematic viscosity [m^2 s^{-1}]
Q	heat generation rate [W]	θ	non-dimensional temperature, $(T - T_c)/(Q/lk_f)$
q_i	heat flux crossing a solid surface [W m^{-2}]	ρ	fluid density [kg m^{-3}].
Ra	Rayleigh number $(g\beta Q l^2/\nu\alpha k_f)$	Subscripts	
R_c	ratio of protrusion thermal conductivity to fluid thermal conductivity, (k_c/k_f)	c	protrusion (chip)
R_s	ratio of substrate thermal conductivity to fluid thermal conductivity, (k_s/k_f)	f	fluid
T	temperature [K]	i	condition at a solid surface
		s	substrate.

mal conductivity on the three-dimensional natural convection flow within the enclosure and on the heat transfer from the protrusion. In applying the results to electronic component cooling, the resultant temperature of the chip is of particular interest, since reliability considerations often determine the design limits. Comparisons with experimental data are also presented, to ascertain whether the numerical scheme is adequately capturing the dominant chip-cooling mechanisms, particularly the effect of substrate conduction.

2. PROBLEM FORMULATION

2.1. *Geometry*

Figure 1(a) illustrates the configuration under study. A single protruding chip (or package hereafter), of dimensions $h_c \times l \times l$, is centered on a substrate of thickness h_s. The chip is assumed to have uniform properties, with internal heat generation rate of Q. The back of the substrate forms one of the vertical walls of a cubical enclosure of side L, filled with a dielectric liquid. The opposite vertical wall is maintained at a constant temperature of T_c, while all other walls of the enclosure, including the back of the substrate, are insulated. This particular geometry is similar to one of the experimental arrangements of Joshi and Paje [23], with which the present computations are compared. Figure 1(b) shows the internal details of the package modeled for the comparisons presented in Section 3.5.

2.2. *Governing equations and non-dimensional parameters*

The non-dimensional governing equations for the three-dimensional problem, assuming constant properties and the Boussinesq approximation, are as follows:

continuity

$$\frac{\partial U}{\partial X} + \frac{\partial V}{\partial Y} + \frac{\partial W}{\partial Z} = 0 \tag{1}$$

x momentum

$$\frac{\partial (UU)}{\partial X} + \frac{\partial (VU)}{\partial Y} + \frac{\partial (WU)}{\partial Z} = -\frac{\partial P}{\partial X} + (Pr/Ra)^{1/2} \cdot \left(\frac{\partial^2 U}{\partial X^2} + \frac{\partial^2 U}{\partial Y^2} + \frac{\partial^2 U}{\partial Z^2} \right) \tag{2}$$

y momentum

$$\frac{\partial (UV)}{\partial X} + \frac{\partial (VV)}{\partial Y} + \frac{\partial (WV)}{\partial Z} = -\frac{\partial P}{\partial Y} + (Pr/Ra)^{1/2} \cdot \left(\frac{\partial^2 V}{\partial X^2} + \frac{\partial^2 V}{\partial Y^2} + \frac{\partial^2 V}{\partial Z^2} \right) + \theta \tag{3}$$

z momentum

$$\frac{\partial (UW)}{\partial X} + \frac{\partial (VW)}{\partial Y} + \frac{\partial (WW)}{\partial Z} = -\frac{\partial P}{\partial Z} + (Pr/Ra)^{1/2} \cdot \left(\frac{\partial^2 W}{\partial X^2} + \frac{\partial^2 W}{\partial Y^2} + \frac{\partial^2 W}{\partial Z^2} \right) \tag{4}$$

Table 1. Selected previous numerical studies involving three-dimensional natural convection

Reference	Aspect ratio†	*Ra*	*Pr*	Code‡	Grid size§	Comments
		Enclosure with bottom heated and top cooled‖				
Aziz and Hellums [6]	1 : 1 : 1	2500–3500	1	T	11 × 11 × 11 U	Solved for perturbation from initial conduction state
Ozoe *et al.* [7]	1 : 1 : 1	4, 6, 8 × 10^3	1, 10	S	9 × 9 × 9 U	Studied flow transitions
Kirchartz and Oertel [8]	10 : 1 : 4	10^3–10^4	0.71	T	41 × 21 × 17 U	Studied stability between flow regimes
Mukutmoni and Yang [9, 10]	2.1 : 1 : 1 : 3.5	4000–3 × 10^4	2.5	T	20 × 20 × 20 U	Studied transitions of steady and oscillating flows
		Enclosure with opposite vertical walls heated and cooled‖				
Mallinson and de Vahl Davis [11]	1 : 1 : 2	10^4–10^6	0.2–100	S	15 × 15 × 15 U	Early study; still used as benchmark for 3-D simulations
Viskanta *et al.* [12]	1 : 1 : 1	10^6	0.2–0.05	S	25 × 25 × 11 U	Low Prandtl number
Lankhorst and Hoogendoorn [13]	1 : 1 : 1 1 : 1 : 2	10^6–10^{10}	0.71	S	30 × 30 × 15 N	k–ε model used for $Ra = 10^{10}$ with 45 × 45 × 20 grid
Fusegi *et al.* [14, 15]	1 : 1 : 1	10^4, 10^6	0.71	T	62 × 62 × 62 U	Ultra-fine grid
		Tilted enclosures with opposite vertical walls heated and cooled‖				
Ozoe *et al.* [16]	2 : 1 : 1	4000	10	T/S	17 × 9 × 9 U	Symmetry at $z = 0$ and L_z simulate infinitely long box
Linthorst and Hoogendoorn [17]	1 : 1 : 1–0.1 : 1 : 10	10^4–10^6	0.71	S		Tilted relative to horizontal 90, 60 and 45°
Yang *et al.* [18]	2 : 1 : 6	4 × 10^4	0.71	T	12 × 12 × 72 U	Studied flow transitions with changes in tilt angle
		Enclosures with discrete heat sources along one wall‖				
Kuhn and Oosthuizen [19]	0.33 : 1 : 2	10^4, 3 × 10^4 and 10^5	0.71	T	22 × 15 × 37 U	Discrete flush heat source on vertical wall
Liu *et al.* [20, 21]	0.15 : 1 : 1.2	8.7 × 10^6	25	T/S	14 × 14 × 46 U	3 × 3 array of discrete protruding heat sources on vertical wall
Chan and Banerjee [22]	2 : 1 : 1		0.7	S	15 × 7 × 7 U	Flush heat source on bottom. All other boundaries at T_c

†Aspect ratio $L_x : L_y : L_z$ refers to coordinate system shown in Fig. 1.
‡Code: S, steady code; T, transient code; T/S, transient code used to obtain steady-state results.
§Grid: U, uniform; N, non-uniform.
‖ Unless otherwise stated, all boundaries not heated or cooled are adiabatic.

energy (fluid)

$$\frac{\partial(U\theta)}{\partial X}+\frac{\partial(V\theta)}{\partial Y}+\frac{\partial(W\theta)}{\partial Z}=(1/Pr\,Ra)^{1/2}\cdot\left(\frac{\partial^2\theta}{\partial X^2}+\frac{\partial^2\theta}{\partial Y^2}+\frac{\partial^2\theta}{\partial Z^2}\right) \quad (5)$$

energy (chip)

$$\left(\frac{\partial^2\theta}{\partial X^2}+\frac{\partial^2\theta}{\partial Y^2}+\frac{\partial^2\theta}{\partial Z^2}\right)+1/R_C H_C=0 \quad (6)$$

energy (substrate)

$$\left(\frac{\partial^2\theta}{\partial X^2}+\frac{\partial^2\theta}{\partial Y^2}+\frac{\partial^2\theta}{\partial Z^2}\right)=0. \quad (7)$$

The appropriate non-dimensional parameters are $Ra = g\beta Q l^2/\alpha\nu k_f$, $Pr = \nu/\alpha$, $U = u/U_0$, $V = v/U_0$, $W = w/U_0$, $U_0 = (g\beta Q/k_f)^{1/2}$, $\theta = (T-T_c)/(Q/lk_f)$, $P = p/(\rho U_0^2)$, $X = x/l$, $Y = y/l$, $Z = z/l$, $H_c = h_c/l$, and $H_s = h_s/l$. We note that the normalization scales for the velocities and temperature involve Q, since it is the driving parameter for the transport. Since the normalized velocities and temperatures are functions of Q additionally through their dependence on Ra, the dimensional changes in the transport variables with Q need to be carefully interpreted.

The boundary conditions at the enclosure walls are as follows:

$$X=0;\quad \frac{\partial\theta}{\partial X}=0,\quad U=0,\quad V=0,\quad W=0$$

$$X=X_L;\quad \theta=0,\quad U=0,\quad V=0,\quad W=0$$

$$Y=0, X_L;\quad \frac{\partial\theta}{\partial Y}=0,\quad U=0,\quad V=0,\quad W=0$$

$$Z=0, X_L;\quad \frac{\partial\theta}{\partial Z}=0,\quad U=0,\quad V=0,\quad W=0$$

where $X_L = L/l$.

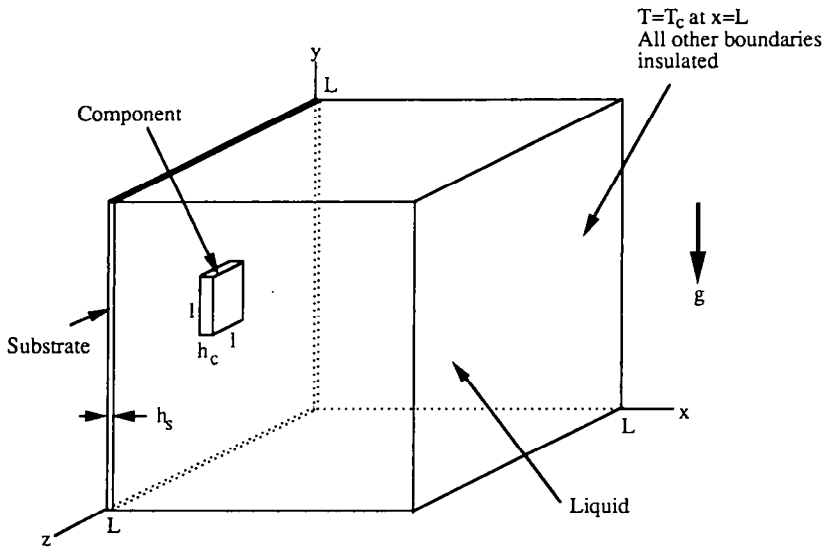

a)

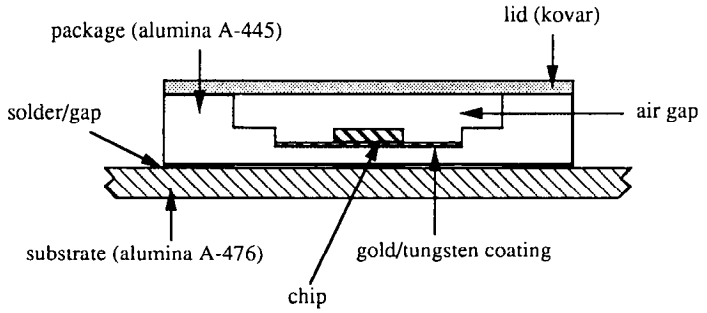

b)

FIG. 1. (a) Geometry of enclosure; (b) internal details of electronic package used in ref. [23].

In addition, the boundary conditions at the interfaces between two different materials are

$$R_i\left(\frac{\partial \theta_i}{\partial X_n}\right)_i = R_j\left(\frac{\partial \theta_j}{\partial X_n}\right)_j, \quad \theta_i = \theta_j,$$

$$U = 0, \quad V = 0, \quad W = 0$$

where X_n is the coordinate along the outward normal of the surface (i.e. $X_n = X$ if the surface is in the Y–Z plane), i and j refer to the two different materials (s for substrate, c for chip, and f for fluid), and $R_s = k_s/k_f$ and $R_c = k_c/k_f$. These are implicitly satisfied in the present computations through the use of the harmonic mean formulation for interface diffusivities, as discussed later.

For this investigation, the geometry of the enclosure was held constant, with $X_L = 5.1$, $H_s = 0.08$, and $H_c = 0.21$. The Prandtl number was chosen as 25, with $R_c = 2360$. This corresponds to the use of fluorinert liquid FC-75 [24] as the coolant with a silicon chip. The Rayleigh number was varied over a wide range from 10^3 to 10^9, assuming $R_s = 575$, which corresponds to an alumina ceramic substrate. A 1 cm square chip operated with a power level of 1.5 W in FC-75 corresponds to a Rayleigh number of approximately 10^9. To study the thermal spreading along the substrate, values of $R_s = 0.5$, 5, and 50 were also employed with $Ra = 10^6$.

A single run was executed for $Ra = 10^9$, $R_s = 575$, and $Pr = 10$. The non-dimensional chip temperature and substrate isotherms were virtually unchanged compared to the same case with $Pr = 25$, suggesting that the current results may also be applied to other liquids. This was also observed by Sathe and Joshi [5] for similar two-dimensional calculations.

In addition to the Rayleigh number defined above,

there are two other modified forms that can be used; (1) $Ra_c = g\beta(T_{chip} - T_c)L^3/\alpha\nu$, a Rayleigh number which is representative of the enclosure for large values of R_s; and (2) $Ra_{bl} = g\beta(T_{chip} - T_c)l^3/\alpha\nu$, which is representative of the boundary layer along the chip itself. The enclosure Rayleigh number can be used to compare the current results with previous studies of enclosures with opposite vertical walls heated and cooled, while the boundary layer Rayleigh number is useful in characterizing the flow near the chip. Note that $Ra_c = Ra\theta_{chip}(X_L)^3$ and $Ra_{bl} = Ra\theta_{chip}$.

2.3. *Numerical method*

The governing equations are discretized using a control-volume approach as described by Patankar [25]. This approach uses control volumes for velocities that are staggered with respect to those for temperature and pressure; power law scheme for the differencing of dependent variables; harmonic mean formulation for the interface diffusivities; and the SIMPLER [25] algorithm for the velocity–pressure coupling. A solution is obtained from an initial guess through an iterative scheme using a line-by-line tridiagonal matrix algorithm. The conjugate conduction in the chip and substrate is handled numerically by solving the same full set of momentum and energy equations throughout the entire enclosure, but with a large value of viscosity specified for the solid regions. Details of the technique can be found in Patankar [25].

The numerical solution is assumed converged when the maximum temperature change during successive iterations is less than 0.00001 × the maximum temperature for that iteration, and when overall energy balances on the enclosure, the chip, and the fluid are obtained within 1%. The use of the maximum changes of the variables as convergence criteria has to be used with caution. As pointed out by Patankar [25], monitoring the changes in dependent variables from iteration to iteration may not be sufficient if under-relaxation is being employed. In the present study, strong under-relaxation is required for the velocities, particularly on the V component because of the strong source term from the buoyancy. On the other hand, temperature required only minor under-relaxation. As a result, the velocity changes from iteration to iteration are somewhat artificial, while the temperature changes are a better reflection of the problem convergence. Thus, although changes in values of the velocities from iteration to iteration were also monitored, along with the overall mass balance, temperature change was used as one of the convergence criteria.

With the conjugate conduction, the solution took much longer for convergence than for a comparable three-dimensional enclosure problem with simple temperature boundary conditions. Typically, 3000–20 000 iterations were needed for convergence, requiring from 200 to 1000 CPU min on an Amdahl 5990/500 mainframe. Use of previously converged solutions at different conditions reduced the run times somewhat.

The solution was obtained throughout the entire enclosure; no symmetry condition was imposed at $Z = X_L/2$. This prevented the forcing of a symmetric solution where one may not exist, as may be the case if the plume above the chip became unsteady. As it turned out, the solutions were indeed symmetric for all conditions examined.

At higher Rayleigh numbers, severe under-relaxation was required to obtain convergence. To determine whether the converged solutions corresponded to physically steady solutions, an unsteady version of the code was used to check the results at the highest Rayleigh number, 10^9. The unsteady code was fully implicit in time, and used the same iteration scheme as the steady version of the code to obtain convergence within a given time step. Convergence for a given time step was assumed when the change in temperature between successive iterations, for all grid points, was less than 0.00001 × the maximum value of temperature at that time step. This criterion resulted in overall energy balances (including the thermal capacitance) within 0.5%. The unsteady non-dimensional equations also led to the introduction of two additional non-dimensional parameters, $C_s = (\rho c_p)_s/(\rho c_p)_f$ and $C_c = (\rho c_p)_c/(\rho c_p)_f$.

The numerical code was validated using a simple three-dimensional cubical enclosure without the substrate and protruding element, and with $\theta = 0$ at $X = 0$ and $\theta = 1$ at $X = 1$. The Rayleigh number was assumed to be 10^6 and the Prandtl number was 0.7, corresponding to one of the cases investigated by Lankhorst and Hoogendoorn [13]. Using a similar (but not identical) 30 × 30 × 15 non-uniform grid, and using the same symmetry assumption, the resulting Nusselt numbers at the hot wall were within 1.5% of those of Lankhorst and Hoogendoorn [13]. In addition, flow patterns and isotherms identical to [13] were observed in both the X–Y and Z–X planes.

3. RESULTS

3.1. *Grid sizing*

When performing three-dimensional numerical simulations, the numerical accuracy must often be compromised to some extent to accommodate practical grid sizes. A review of prior studies in Table 1 reveals that, with the exception of Fusegi *et al.* [14, 15], the grids that were employed would be considered fairly coarse for two-dimensional studies. Although such grids invariably miss some of the finer details of the flow structures, they can still be tailored to provide reasonable estimates of the key features of the flow (Yang *et al.* [18]). In the present study, the grid-sizing problem is compounded by four other factors: (1) the need to capture the flow around the chip; (2) the wide range of Rayleigh numbers under consideration; (3) the requirements of proper grid spacing near interfaces of materials with vastly different thermal con-

ductivities; and (4) the large Prandtl number, resulting in thinner thermal boundary layers compared with momentum boundary layers.

The third point listed above proved to be a particular problem. For the large value of R_s used in the base case, only a single control volume was used in the X-direction for the thin substrate. Attempts to use more than one led to problems with round-off error for the control volume at the interface between the substrate and the fluid, due to the very small temperature changes in the substrate. As a result, the overall energy balance would not converge. For lower values of R_s, two control volumes were used in the X-direction with no convergence problems.

Most of the results presented here were obtained using a $23 \times 22 \times 22$ or a $24 \times 22 \times 22$ non-uniform grid. Several points were chosen near the hot and cold surfaces to capture the thermal boundary layers. These points were often adjusted slightly for various Rayleigh number ranges (i.e. more points closer to the wall for higher Rayleigh numbers). Below $Ra = 10^5$, the grid in the remainder of the flow was fairly uniform. At higher Rayleigh numbers, in which the boundary layer regions accounted for smaller portions of the enclosure, several intermediate grid points were located between the thermal boundary layer and the core of the flow, to capture the outer region of the momentum boundary layer. The grid spacing within the core of the enclosure was relatively coarse.

At $Ra = 10^9$, several finer grids were also used to check the results of the base grid. The finer grids used the symmetry condition at $Z = X_t/2$, which was justified based on the symmetry observed in full enclosure results with the base grid. Table 2 compares conditions at the hot surfaces obtained for the base grid with those found using a $31 \times 26 \times 16$ grid, which used more intermediate grid points, and a $37 \times 30 \times 20$ grid, which used more interior grid points as well. The relatively small differences between the various grids indicate that the highly non-uniform base grid was sufficient for capturing the heat transfer characteristics at the hot surfaces.

3.2. *Effect of Rayleigh number* ($R_s = 575$)

To describe the three-dimensional nature of the flow and heat transfer, data for a few selected planes are shown in Figs. 2 and 3 for $Ra = 10^3$, 10^6 and 10^9. Figure 2 shows the U–V velocity vectors and the isotherms for the X–Y plane at $Z = 2.55$ (i.e. the symmetry plane). At $Ra = 10^3$, Fig. 2(a), the primary flow is in the X–Y plane and is characterized by a single cell that is disturbed only slightly near the protruding chip. The isotherms at $Ra = 10^3$ in Fig. 2(a) indicate that the relatively strong U velocities convect low temperature fluid from the cold wall towards the hot wall in the lower portion of the cavity and high temperature fluid from the hot wall towards the cold wall in the upper portion. This leads to larger temperature gradients (in the x-direction) at the bottom of the hot wall and the top of the cold wall and reduced gradients at the top of the hot wall and the bottom of the cold wall. Note that the chip is nearly isothermal, mainly as a result of the high R_c.

When $Ra = 10^6$, Fig. 2(b), a cellular flow is also evident, but the bulk of the primary flow in the vertical direction is confined to boundary layers along the hot and cold surfaces, rather than spreading throughout the enclosure as seen at $Ra = 10^3$. These boundary layers thicken significantly near the lower and upper walls due to three-dimensional effects of the horizontal walls. The flows around the upper and lower corners of the chip lead to weak jets of fluid moving towards the substrate at the top of the chip and away from the substrate near the bottom of the chip. The effect of the flow on the isotherms is similar to Fig. 2(a), but with the temperature gradients confined to thermal boundary layers along the hot and cold wall. The cross convection (between the cold and hot walls) seems to be important only near the top of the hot wall and the bottom of the cold wall. The remainder of the core of the enclosure, between the boundary layers, can be characterized as well stratified.

At $Ra = 10^9$, Fig. 2(c), the vertical primary flow is confined to even thinner boundary layers near the hot and cold walls. The vertical velocities are much greater in the region near and above the chip compared to that along the substrate or the cold wall. In particular, the velocities in the plume from the top of the chip are much higher than the rest of the flow. There is still a weak cellular structure to the primary flow. Like the $Ra = 10^6$ case, most of the horizontal flow between the hot and cold boundary layers occurs in regions

Table 2. Effect of grid size on heat transfer from hot surfaces for $Ra = 10^9$ and $R_s = 575$

	$24 \times 22 \times 22$	$31 \times 26 \times 16$†	$37 \times 30 \times 20$†
Heat loss from:			
face	0.133	0.135	0.136
top	0.016	0.018	0.018
bottom	0.037	0.035	0.034
sides	0.048	0.056	0.060
substrate	0.763	0.751	0.750
Maximum chip temperature	0.00735	0.00723	0.00742

†$31 \times 26 \times 16$ and $37 \times 30 \times 20$ grids cover region from $Z = 0$ to 2.55, assuming symmetry about $Z = 2.55$. For full domain, these represent grid sizes of $31 \times 26 \times 29$ and $37 \times 30 \times 36$.

near the top and bottom walls, but with velocities less than 10% of the maximum vertical velocity. The isotherms in Fig. 2(c) reveal very steep gradients near the hot and cold surfaces and a well stratified core. The cross convection is negligible everywhere. Details of the flow near the chip, Fig. 2(d), present a clearer view of the growing thermal boundary layer along the chip face.

Velocity vectors and isotherms for the Y–Z plane at $X = 0.185$ (through the center of the chip) are shown in Fig. 3. These plots are composite drawings which take advantage of the symmetry about $Z = 2.55$, with isotherms shown on the right and velocity vectors shown on the left of each plot. The V velocity component near the substrate is fairly constant in the Z-direction, except in the vicinity of the sidewalls for $Ra = 10^3$ in Fig. 3(a). The W velocity component near the substrate is outwards, towards the side walls, near the bottom of the enclosure and inwards near the top of the enclosure.

At $Ra = 10^6$, Fig. 3(b), the strength of the primary flow (in the Y-direction) again remains fairly constant

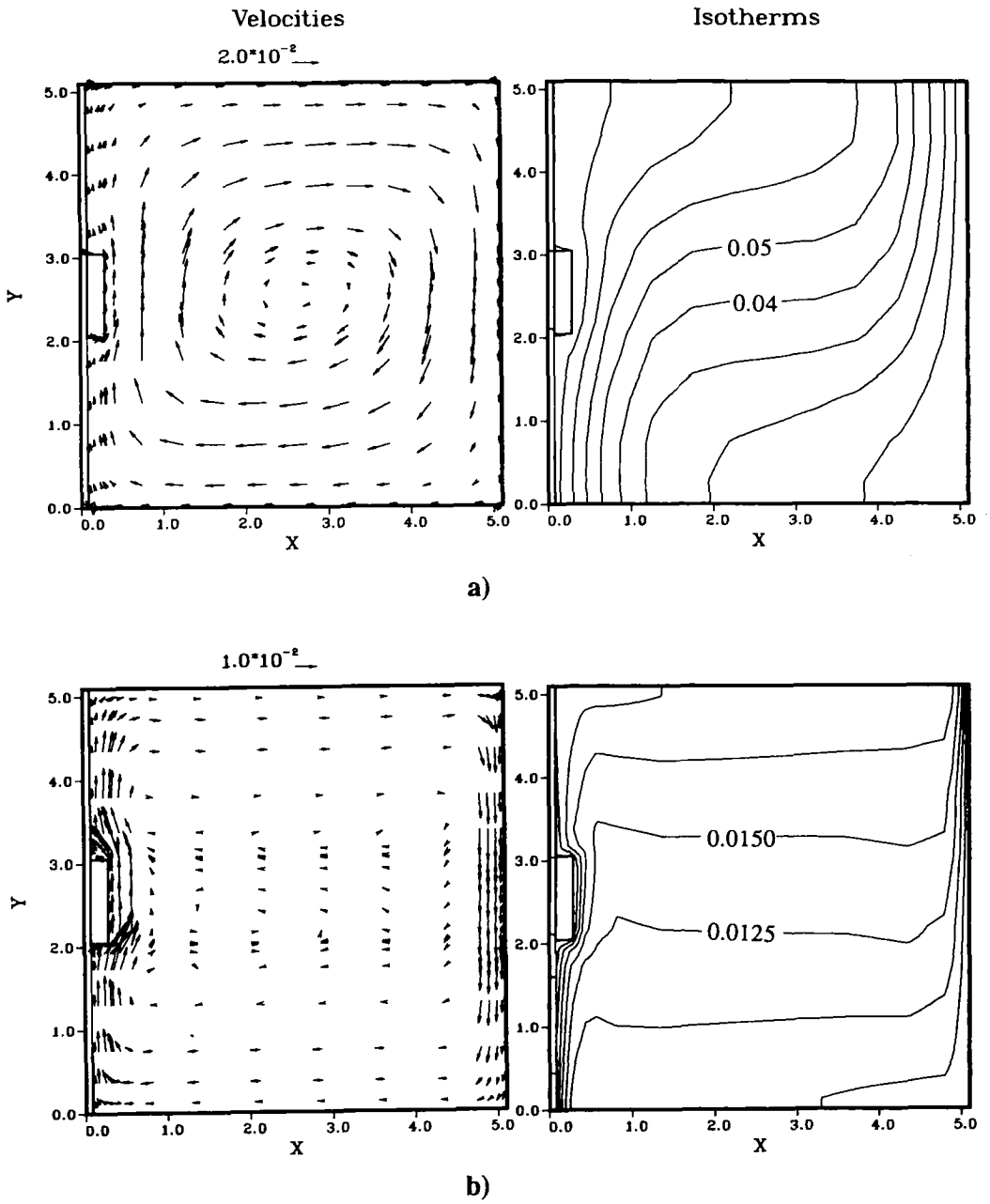

FIG. 2. U–V velocity vectors and isotherms for the X–Y plane at $Z = 2.55$ for $R_s = 575$: (a) $Ra = 10^3$; (b) $Ra = 10^6$; (c) $Ra = 10^9$; (d) detail near chip for $Ra = 10^9$.

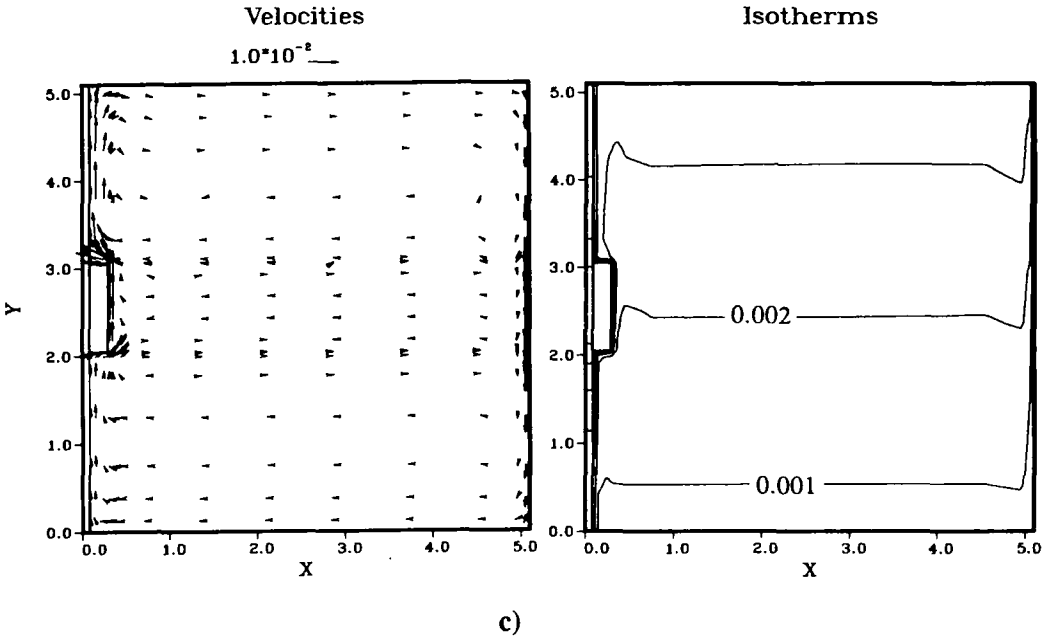

FIG. 2.—*Continued.*

across the Z-direction, with a smaller region of diminishing strength near the side walls. The one exception to this is the region above the chip, where the flow is slightly stronger than that along the rest of the substrate. This is a result of the emergence of a plume from the top of the chip. Near the upper edge of the substrate directly above the chip, the W velocity component is outwards, rather than inwards as in Fig. 3(a), as this plume encounters the solid top surface. At $Ra = 10^9$, Fig. 3(c), the plume grows to dominate the primary flow. When it reaches the top wall, it spreads horizontally outwards towards the side walls, as well as towards the cold wall, creating a small circular region of very strong secondary velocities.

The isotherms in Fig. 3 reveal spreading of the heat away from the chip in a non-symmetrical manner for all three *Ra*. Also seen is the formation of a thin thermal boundary layer type region around the chip with increasing *Ra*. The thermal stratification in the enclosure liquid below the chip becomes evident with increasing *Ra*.

Figure 4 shows isotherms and Nusselt numbers along the substrate surface and along the various chip

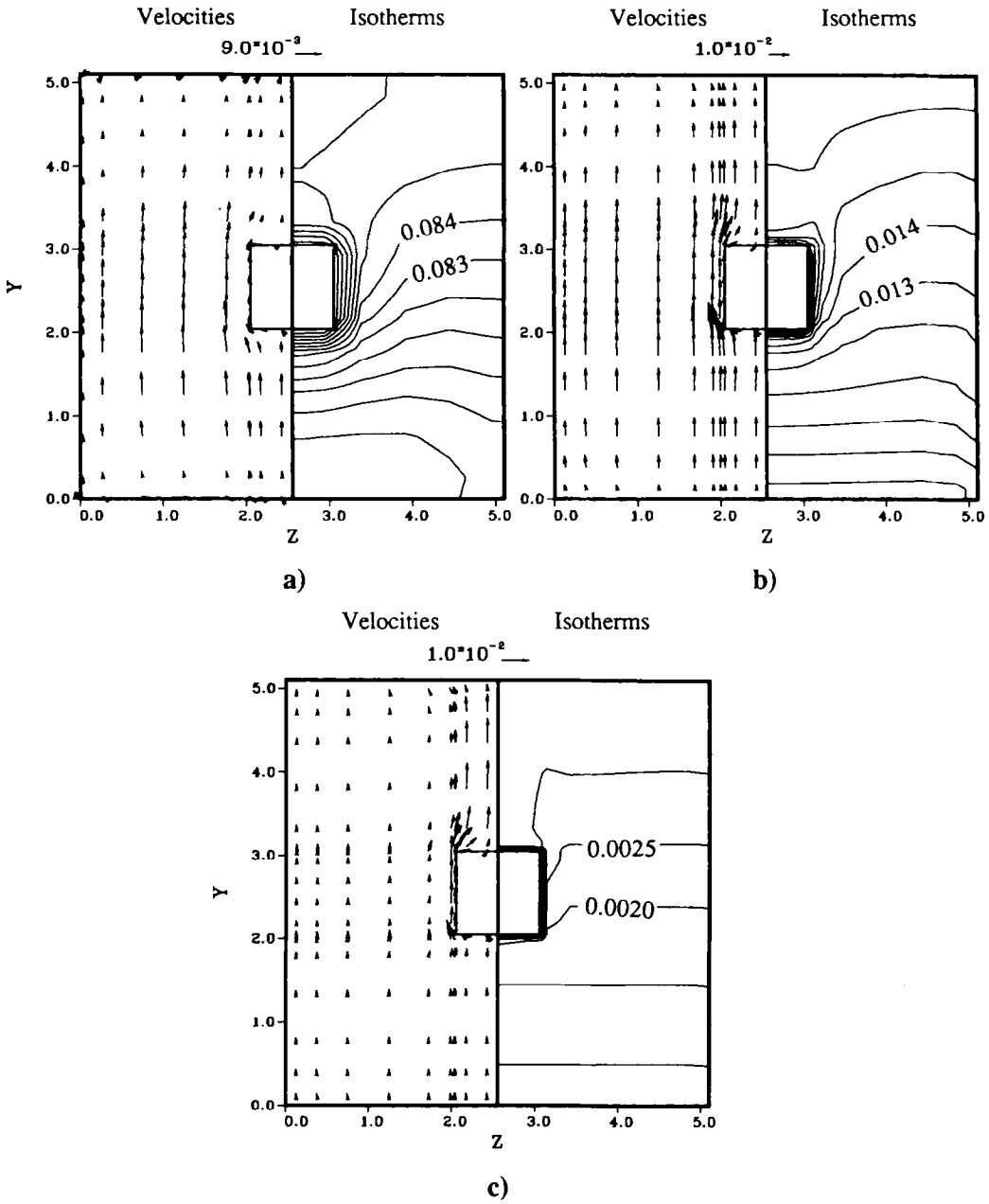

FIG. 3. W–V velocity vectors and isotherms for the Z–Y plane at $X = 0.185$ for $R_s = 575$: (a) $Ra = 10^3$; (b) $Ra = 10^6$; (c) $Ra = 10^9$.

surfaces for $Ra = 10^3$, 10^6 and 10^9. The Nusselt number is calculated as

$$Nu = \frac{q_i L}{k_f(T_i - T_c)} = \frac{(\partial\theta/\partial X_n)_i X_L}{\theta_i}$$

where the subscript i refers to the condition at the particular surface. The contour plots in Fig. 4 are also composite drawings which take advantage of the symmetry of the flow, with the isotherms shown on the left-hand side of each drawing and the Nusselt number contours shown on the right. It should be noted that the Nusselt number is undefined along the edges of the chip. The values of Nu indicated by the contour plots at these edges reflect the values at the nearest numerical node.

For $Ra = 10^3$, the maximum Nusselt numbers on the substrate occur near the bottom, where the cross convection has thinned the thermal layer near the hot wall. Similarly, the upper region of the substrate, where the cross convection is away from the wall, is where the lowest Nusselt numbers are found. Note that there is a region around the chip along the sub-

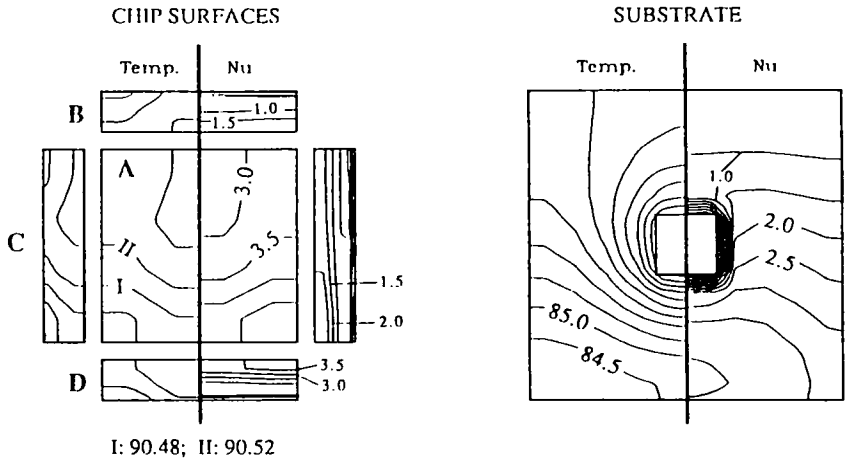

a)

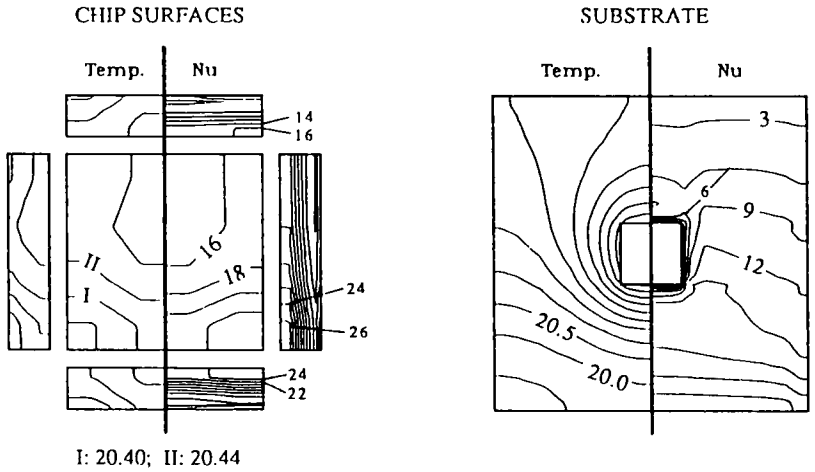

b)

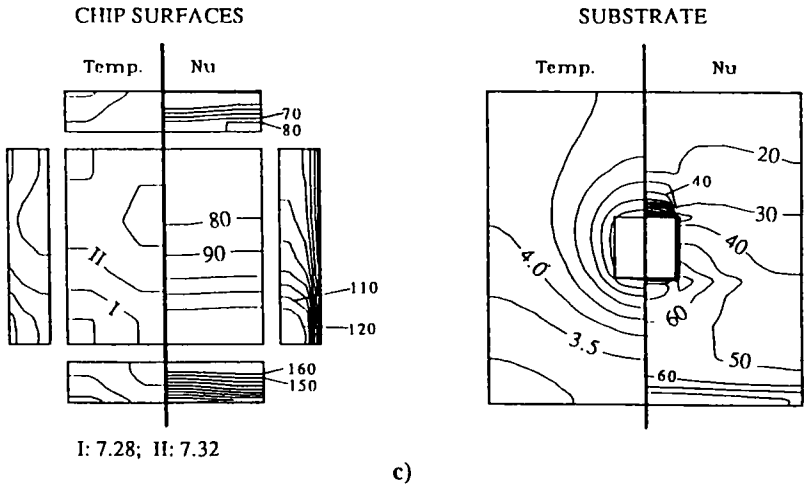

c)

FIG. 4. Temperature and Nusselt number contours along substrate and chip surfaces: (a) $Ra = 10^3$; (b) $Ra = 10^6$; (c) $Ra = 10^9$. Chip surfaces marked on (a); A = front face, B = top, C = side, D = bottom. Values of isotherm contours are multiplied by 1000.

strate, inside the contour marked 1.0 in Fig. 4(a), where the Nusselt numbers are negative, indicating that the fluid heated by the chip is transferring heat to the substrate. The viscous effect near the side walls, which leads to reduced primary flow, is evident from the lower Nusselt numbers near the outer edges of the substrate.

On the chip surfaces, values of Nu are larger than those along the substrate. In particular, with the exception of $Ra = 10^3$, the maximum values occur on the bottom surface, where the flow along the lower substrate impacts the chip. At $Ra = 10^3$ flow along the bottom face is relatively weak resulting in Nu values comparable to the chip front face. Along the front face of the chip, the Nusselt numbers are highest at the bottom, where the growing boundary layer is at its thinnest.

Three-dimensional effects are also evident along the front face, with higher heat transfer coefficients near the side edges compared to the center. The temperature varies little across the chip surfaces (the isotherms shown in the figure are only 4×10^{-5} apart). This, combined with the fact that a similar effect was observed by Kuhn and Oosthuizen [19] for a flush-mounted, isothermal element, suggests that the higher Nu values near the edges are a result of increased surface heat transfer rates, rather than lower surface temperatures. The increased heat transfer rates near the edge are likely to be a result of greater thermal transport in the near-surface flow provided by the spanwise temperature gradients.

The relatively low values of the Nusselt numbers for the chip surfaces, combined with the relatively large substrate thermal conductivity, result in significant conduction through the substrate. The isotherms reflect this behavior, showing only a 5% drop in surface temperature from the chip to the edge of the substrate. The relatively isothermal substrate surface is the reason that the primary flow strength does not drop off significantly across the substrate.

The patterns of the isotherms along the substrate reflect three key mechanisms: (1) conduction through the substrate will lead to reduced temperature variations across the surface; (2) variations in heat transfer coefficients along the substrate will lead to increased variations in the temperature; and (3) the stratified nature of the temperature field, which also affects the heat transfer coefficients, will lead to temperature variations in the vertical direction. The oval-shaped isotherms around the chip reflect the latter two effects.

The Nu patterns along the substrate and the chip surfaces are somewhat similar for $Ra = 10^6$, but with values at least five times greater in magnitude than those at $Ra = 10^3$. The reduced thermal resistances along the chip surfaces leads to a greater percentage of heat loss directly to the fluid, and subsequently, less conduction and spreading through the substrate. This behavior is again evident in the isotherm contours, where the drop in temperature from the chip to the edge of the substrate is now 17%. The three-dimensional effects along the various chip faces are also similar to those seen at $Ra = 10^3$. The region of negative Nu values on the substrate near the chip is very small, and is seen on Fig. 4(b) as the dark region around the chip where the gradients of Nu are very large.

At $Ra = 10^9$, the Nusselt numbers along the chip are up to $20\times$ higher than at $Ra = 10^3$, leading to even greater heat loss directly to the fluid and reduced substrate conduction. The result is larger temperature differences between the chip and the substrate (45% drop in temperature between the chip and the outer edge of the substrate), which accounts for the relative dominance in the primary flow by the plume above the chip.

The three-dimensional effect along the chip front face is almost negligible at $Ra = 10^9$. The temperature gradients normal to this face are already quite high, due to the thin boundary layer, so the spanwise gradients due to the three-dimensional effect do not lead to a significant increase in thermal transport near the edges. This trend is also similar to the one reported by Kuhn and Oosthuizen [19].

Figure 5 presents the fractions of the net generated power that are lost from the various chip surfaces, the maximum chip temperature and the temperature of the substrate at $Z = 1.125$ and $Y = 2.55$, as a function of Rayleigh number. Because of the large value of the ratio of substrate-to-fluid thermal conductivity, conduction through the back of the chip to the substrate accounted for most of the total heat loss from the chip—over 90% at $Ra = 10^3$ decreasing to 76% at $Ra = 10^9$. The heat loss from the front face was the next largest, and increased with Rayleigh number as a result of the increase in the heat transfer coefficients. The other four surfaces of the chip accounted for almost negligible heat loss at $Ra = 10^3$ (as can be seen in the insert in Fig. 5(a)), with substantial relative increases with increasing Rayleigh number.

The non-dimensional chip temperature decreased by more than an order of magnitude from 0.101 for $Ra = 10^3$ to 0.00735 for $Ra = 10^9$. For comparison, the chip temperature for the conduction only solution was 0.21. Figure 5(b) also shows how the reduction in substrate conduction at higher Rayleigh numbers led to a greater difference between the substrate and chip temperatures.

3.3. *Validity of steady solution at* $Ra = 10^9$

Because severe under-relaxation was used to obtain results at high Rayleigh numbers, the validity of the steady solution was further investigated. Lage and Bejan [26] simulated a two-dimensional enclosure with opposite vertical walls heated and cooled and were able to obtain laminar solutions for enclosure Rayleigh numbers up to 10^{11} for a Prandtl number of 10. Based on these results and a compilation of experimental results, they suggest a relation for the transition Rayleigh number of the form $Ra = 10^9\ Pr$.

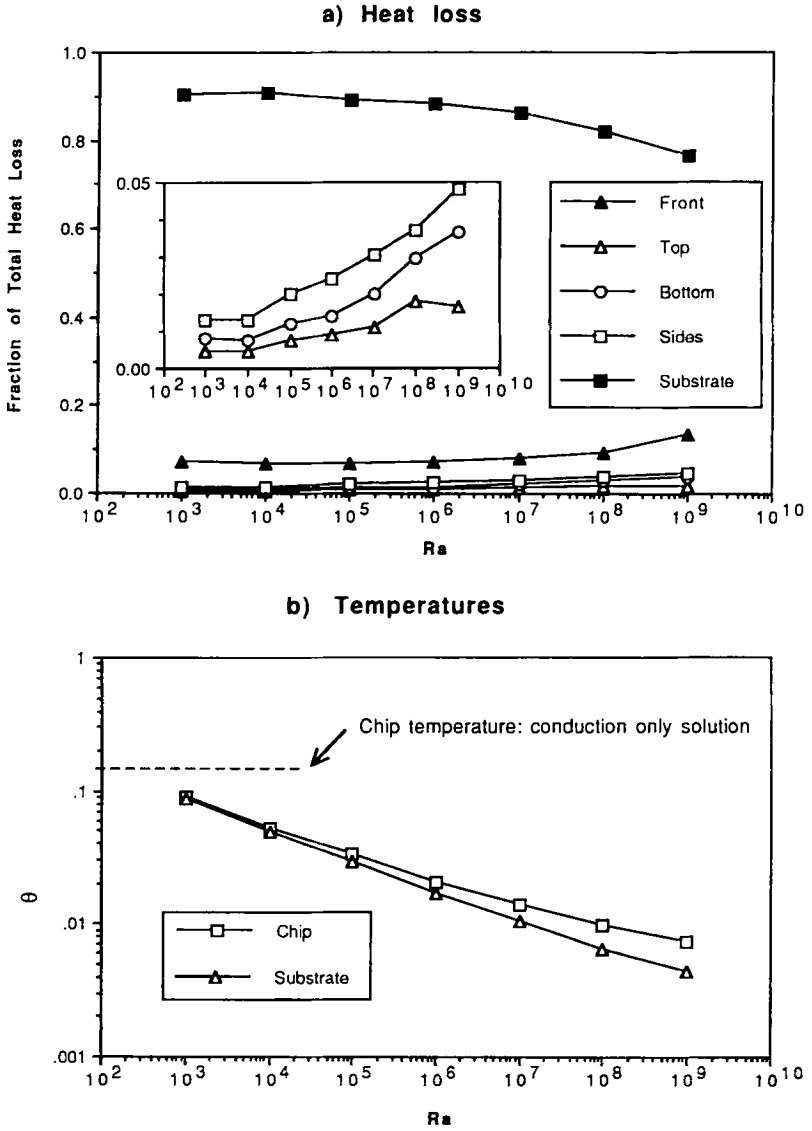

FIG. 5. Effect of Rayleigh number on: (a) fraction of heat loss from the hot surfaces (chip and substrate); and (b) maximum temperature of chip and temperature of substrate at $Z = 1.125$ and $Y = 2.55$.

The $Ra = 10^9$ case presented here corresponds to an enclosure Rayleigh number of 2×10^8, suggesting that a steady solution would be possible, at least for the simple enclosure problem. However, the effect of the protruding chip must also be considered. In this regard, Liu *et al.* [21] found oscillatory, long-time solutions for a three-dimensional simulation of a 3×3 array of protruding chips in a dielectric liquid at $Ra = 2 \times 10^{10}$ (using the same definition of Rayleigh number employed here). The oscillations were assumed to be a result of the formation of secondary cells. However, these results were obtained by specifying a constant heat flux at the chip surfaces, and ignoring the heat capacity of the chips. In addition, oscillations were not observed in experimental results from a similar configuration (Kelleher *et al.* [3]). In light of these considerations, the steady solution obtained at $Ra = 10^9$ appeared valid.

As a more definitive check of whether the present solution obtained at $Ra = 10^9$ represented a physically steady solution, an unsteady version of the three-dimensional code was utilized. The solution from the steady code was input as the initial condition for the unsteady run, to determine whether oscillations would arise. Values of C_s and C_c were specified at 1.64 and 0.90, characteristic of an alumina substrate and a silicon chip. The unsteady code was run for 1000 non-dimensional time units with a time step of one. The total simulation time corresponded to approximately six times the period of oscillations observed by Liu *et al.* [21]. Changes in the velocity and temperatures, which were monitored for each

time step, revealed monotonically decreasing values rather than cyclic changes which might suggest oscillations. Final results from the unsteady run after 1000 time steps, including substrate and chip temperatures and heat fluxes, differed from the initial conditions by less than 1%. This exercise proved that results of the steady code did represent a true steady state, at least for the specific values of C_s and C_c employed here.

3.4. *Effect of substrate thermal conductivity* ($Ra = 10^6$)

The velocity vectors and isotherms in the X–Y plane at $Z = 2.55$ are shown in Fig. 6 for $Ra = 10^6$ and $R_s = 0.5$ and 50. (The flow patterns and isotherms for $R_s = 5$ are not substantially different than those at $R_s = 0.5$, so these are omitted for brevity.) At $R_s = 50$, Fig. 6(a), there is reduced flow in the lower portion of the enclosure compared to $R_s = 575$ (base case shown in Fig. 2). The isotherms reveal that there is less spreading below the chip, and thus less driving force for buoyant flow along the lower substrate surface. The temperature of the chip itself, as well as the temperature gradients near the chip, have increased. Note that the temperatures in the core of the enclosure are quite similar to those of the base case.

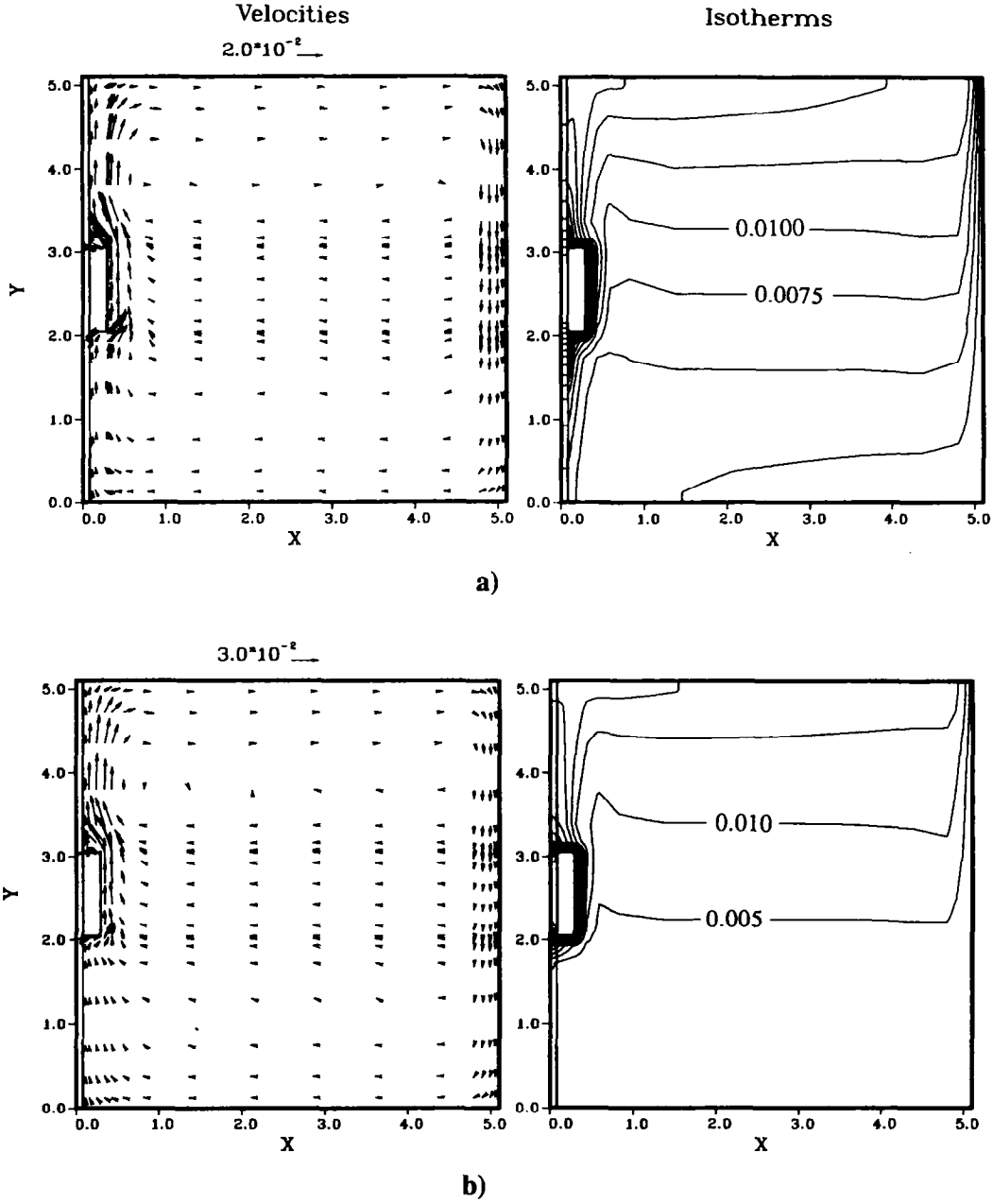

FIG. 6. U–V velocity vectors and isotherms for the X–Y plane at $Z = 2.55$ for $Ra = 10^6$: (a) $R_s = 50$; (b) $R_s = 0.5$.

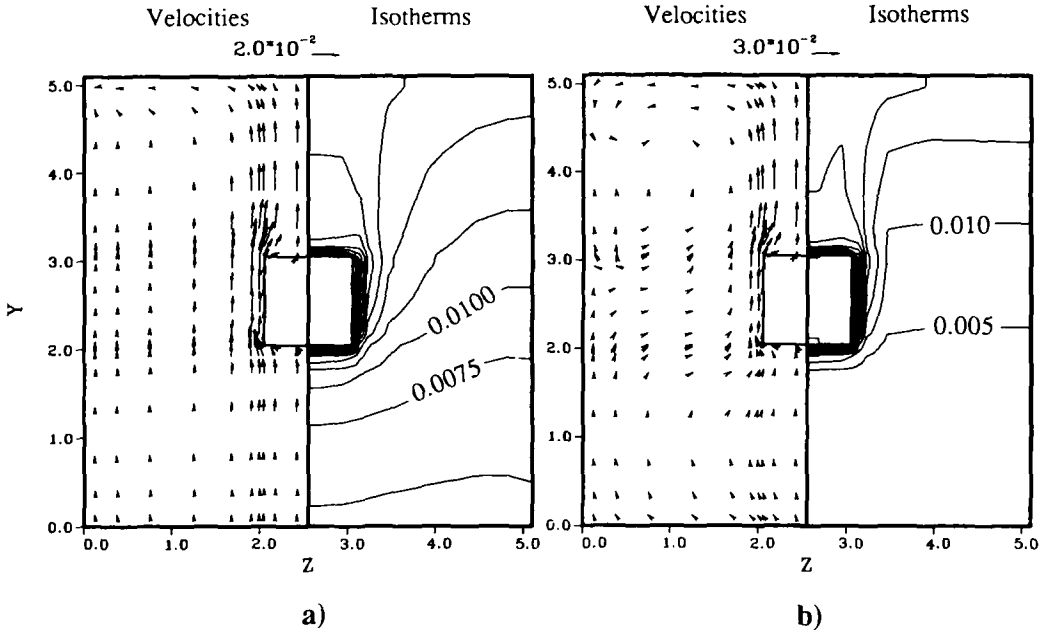

FIG. 7. W–V velocity vectors and isotherms for the Z–Y plane at $X = 0.185$ for $Ra = 10^6$: (a) $R_s = 50$; (b) $R_s = 0.5$.

At $R_s = 0.5$, Fig. 6(b), the flow is almost entirely confined to the upper half of the enclosure, with nearly isothermal conditions across the bottom half. The plume strength has increased even more, with maximum velocities over twice as large as those observed in the base case. The isotherms reveal minimal spreading through to the lower region of the substrate.

In Fig. 7 the W–V velocity vectors and isotherms are shown for the $X = 0.185$ plane. For $R_s = 50$, there is still some moderate flow along the substrate, but this decreases rapidly in the outer-edge regions. The increased strength of the plume above the chip can be seen, along with the outward flow resulting from the plume encountering the upper wall. As R_s drops to 0.5, the flow in the $X = 0.185$ plane becomes dominated by the boundary layers along the chip side and the plume above the chip. The interaction of the very strong plume with the upper wall leads to a secondary swirling cell.

The Nusselt numbers and isotherms along the substrate and chip surfaces (Fig. 8) give further evidence to the effect of substrate thermal conductivity. Compared to the base case, the Nusselt numbers for $R_s = 50$ are lower along most of the substrate, but higher on and near the chip. This is due to the higher temperatures on the chip surfaces, which amount to an increase in the boundary layer Rayleigh number and thus more vigorous flow. A region of negative Nusselt number is observed near the upper edge of the enclosure (above the contours marked 0 in Fig. 8(a)), where the plume is heating the substrate. The isotherm patterns resemble those of the base case, but with a much larger drop from the chip to the substrate edge (69%).

The Nusselt numbers for $R_s = 0.5$, Fig. 8(b), are negligible along the substrate, except directly around the chip. The values on the chip surfaces themselves have increased further, as a result of the higher chip temperature and thus more vigorous flow. Along the substrate above the chip, the Nusselt numbers have decreased to near zero, and the region of negative values has grown considerably. This behavior is attributed to the combination of the stronger plume and reduced conduction through the substrate. The isotherm pattern is substantially different than those seen at higher values of R_s. The elevated temperatures along the side regions correspond to the stratified flow in the core, while the large funnel-shaped region above the chip results from the heating by the plume.

The decrease in the thermal conductivity of the substrate has a profound effect on the surface heat loss fractions, as seen in Fig. 9(a). As R_s is reduced, the fraction of loss through the substrate falls, while fractions from the various chip surfaces increase. At $R_s = 5$, the heat loss from the front face is the largest, while the substrate fraction has dropped to only 14%. At $R_s = 0.5$, the substrate loss is only 1%.

The chip temperature increases substantially with decreasing R_s. As seen in Fig. 9(b), it increases from 0.02 for the baseline case to 0.06 for $R_s = 5$. For $R_s < 5$, further reductions of R_s lead to only moderate increases in chip temperature, since substrate conduction plays a minor role.

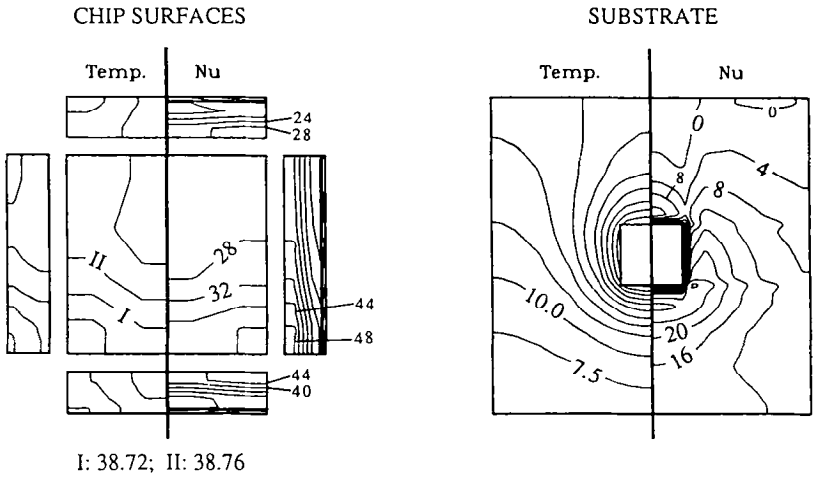

a)

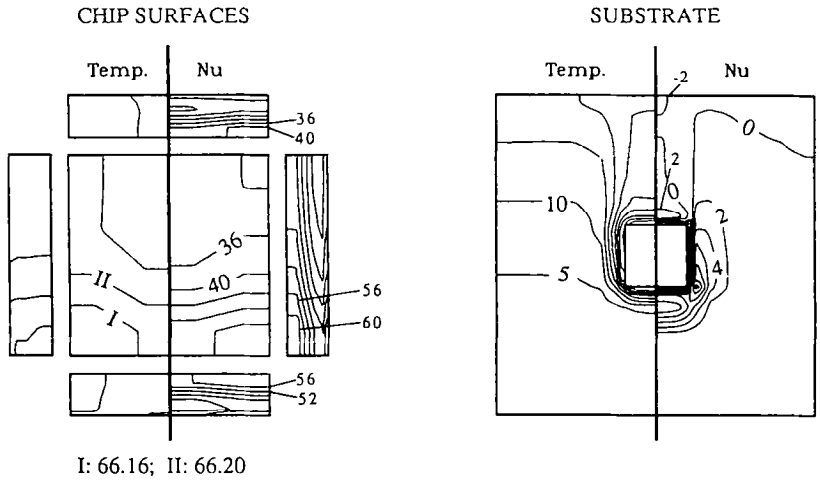

b)

FIG. 8. Temperature and Nusselt number contours along substrate and chip surfaces: (a) $R_s = 50$; (b) $R_s = 0.5$. Values of isotherm contours are multiplied by 1000. See Fig. 4 for chip surface legend.

3.5. *Comparison with experiments*

As mentioned above, the geometry employed here was similar to one of the two configurations in the experiments performed by Joshi and Paje [23]. A key difference was that in the experiments the uniform heat generation was confined to the 1.52 mm square, 0.4 mm thick silicon chip (or 'die' as it is often referred to). This was located within a 20 pin 'leadless chip carrier' package 8.9 mm square and protruding 1.9 mm from the substrate, shown in Fig. 1(b). The die was attached to the ceramic package through thin layers of gold and tungsten. An air space between the die and the lid of the package (made of kovar alloy) provided an additional internal resistance to heat transfer. The package itself was elevated slightly above the substrate, resting only on the 20 solder joints. Measurements of steady temperatures on the chip and selected substrate locations were reported in three dielectric liquids for a range of power levels.

The 3-D code was run for this particular package design with a power level of 1.84 W with FC-75 as the coolant. A slightly modified form of equation (6) was used to prescribe the heat generation only within the chip. Using properties evaluated at the mean temperature between the lid and the cold wall (from the experiments), this corresponded to $Ra = 1.15 \times 10^9$ and $Pr = 24$. Comparisons of measured substrate and chip temperatures with the computations are shown in Table 3. With the exception of the substrate temperature directly behind the package, the results are within -9 and $+15\%$. Given the complicated design of the package, which could not be modeled in all its detail, and the uncertainty associated with the contact resistance between the package and the substrate,

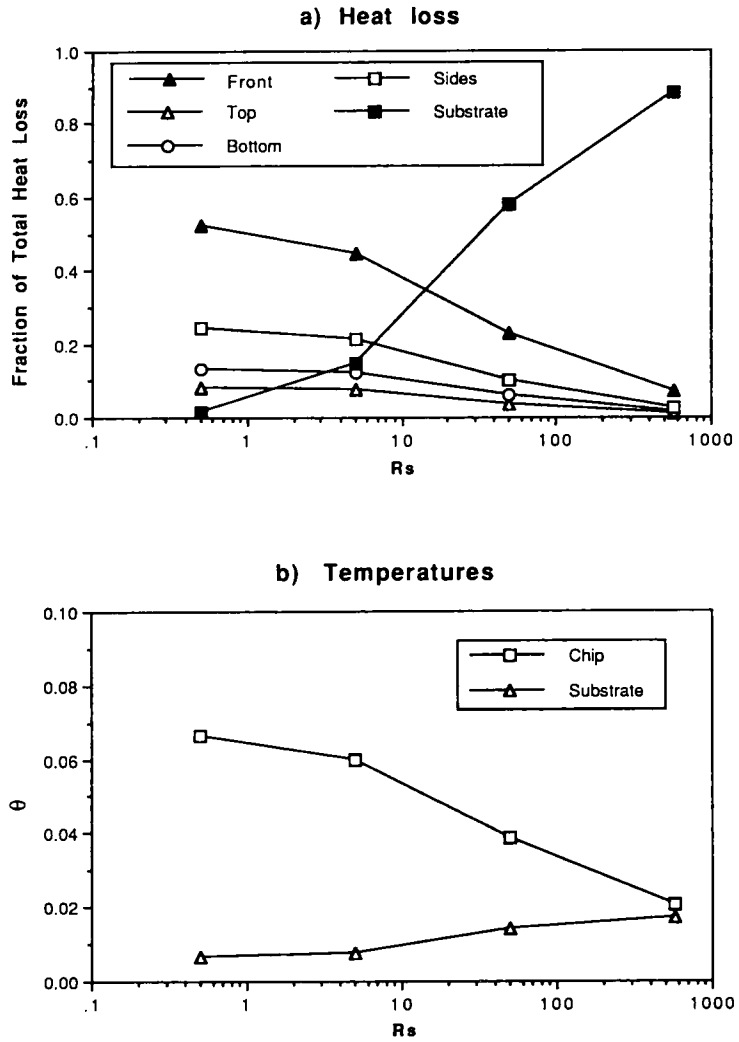

FIG. 9. Effect of substrate thermal conductivity on: (a) fraction of heat loss from the hot surfaces (chip and substrate); and (b) maximum temperature of chip and temperature of substrate at $Z = 1.125$ and $Y = 2.55$.

these results are satisfactory. In particular, the main patterns of the isotherms along the substrate for the numerical results, similar to those shown in Fig. 4(c), are akin to those observed in the experiments using liquid crystals [23].

The numerical simulation revealed very large temperature gradients along the substrate in the Y- and Z-directions directly behind the package, the region where a large discrepancy (35%) was observed between the numerical and experimental results. In

Table 3. Comparison of numerical and experimental results for leadless chip carrier package

Location	θ experiment	θ numerical	Percentage difference
Chip	0.00197	0.0226	+15
Substrate†			
4. ($Z = 2.55$, $Y = 3.98$)	0.0043	0.0048	+12
5. ($Z = 2.55$, $Y = 2.55$)	0.0072	0.0097	+34
6. ($Z = 2.55$, $Y = 1.12$)	0.0032	0.0029	−9
7. ($Z = 1.12$, $Y = 3.95$)	0.0033	0.0037	+12
8. ($Z = 1.12$, $Y = 2.55$)	0.0035	0.0039	+11

†Numbers designate references to thermocouples used by Joshi and Paje [23].

the experiments, three factors could have led to locally increased spreading in this region, which might account for the lower measured temperatures. First, a high thermal conductivity paste was used to attach the thermocouple to the substrate and the size of this connection was sufficient to cover a region where the numerical results showed large temperature variations. Second, behind the substrate was a slab of Plexiglas, which might also have acted as an additional thermal path for spreading. In addition, heat loss from the edges of the enclosure might have resulted in lower temperature throughout the entire enclosure. This may explain why most of the numerically predicted temperatures are above those measured experimentally.

4. CONCLUSIONS

A three-dimensional numerical study was performed to investigate the heat transfer and flow field arising from a heated protruding element mounted on a substrate which formed a vertical wall of a cubic enclosure filled with a dielectric liquid. The characteristics of the flow within the enclosure are dependent on Rayleigh number and substrate thermal conductivity. At $Ra = 10^3$, a single flow cell is observed, disturbed only slightly by the chip. At $Ra = 10^6$, the flow is confined to regions near the surfaces, particularly in the vertical direction, with the flow around the chip creating weak disturbances that extend well into the core of the enclosure. At $Ra = 10^9$, the vertical boundary layer regions become even thinner, with more intense disturbances caused by the flow near the chip and the presence of a strong plume above the chip. As R_s is decreased, the flow becomes more confined to the upper region of the enclosure and the plume above the chip becomes more pronounced.

Conduction through the substrate plays a dominant role in the cooling of the chip for values of R_s greater than 10. At $R_s = 575$, it accounts for over 90% of the total heat loss from the chip for $Ra = 10^3$, dropping to 75% at $Ra = 10^9$. As R_s is reduced, substrate conduction becomes less important while the front face and side heat losses play a more critical role. As substrate conduction becomes less important, at higher Ra and lower R_s, a greater temperature difference develops between the chip and the substrate surface, leading to more vigorous flow near the chip. In the case of reduced values of R_s, it also leads to substantial increases in the chip temperature.

The three-dimensional effects of the flow are most important when a strong plume is present, due to the secondary flow which arises from the interaction of the plume with the upper surface and to the secondary flow which feeds into the plume. The three-dimensional flow effects of the enclosure side walls seem to be relatively weak. Three-dimensional heat transfer effects play a key role in the cooling of the chip, through the increased spanwise temperature gradients near the sides of the chip face, through the chip side heat loss, and through the spanwise conduction in the substrate. The first two effects are most important at lower values of R_s while the latter is crucial at high values of R_s.

Acknowledgements—The authors are grateful for the support of this study through a grant from the Naval Surface Warfare Center, Crane, Indiana under the SHARP effort. The original version of the steady-state three-dimensional code was developed by Dr S. B. Sathe.

REFERENCES

1. A. Bar-Cohen, Thermal management of electronic components with dielectric liquids, *Proc. ASME/JSME Thermal Engng Joint Conf.*, Vol. 2, pp. xv–xxxix (1991).
2. K. A. Park and A. E. Bergles, Natural convection heat transfer characteristics of simulated microelectronic chips, *ASME J. Heat Transfer* **109,** 90–96 (1987).
3. M. D. Kelleher, R. H. Knock and K. T. Yang, Laminar natural convection in a rectangular enclosure due to a heated protrusion on one vertical wall. Part I: experimental investigation, *Proc. 2nd ASME-JSME Joint Thermal Engng Conf.*, Vol. II, pp. 169–178 (1987).
4. M. Keyhani, V. Prasad and R. Cox, An experimental study of natural convection in a vertical cavity with discrete heat sources, *ASME J. Heat Transfer* **110,** 616–624 (1988).
5. S. Sathe and Y. Joshi, Natural convection arising from a heat generating substrate-mounted protrusion in a liquid-filled two-dimensional enclosure, *Int. J. Heat Mass Transfer* **34,** 2149–2163 (1991).
6. K. Aziz and J. D. Hellums, Numerical solution of the three-dimensional equations of motion for laminar natural convection, *Phys. Fluids* **10,** 314–324 (1967).
7. H. Ozoe, K. Yamamoto, S. W. Churchill and H. Sayama, Three-dimensional numerical analysis of laminar natural convection in a confined fluid heated from below, *J. Heat Transfer* **98,** 202–207 (1976).
8. K. R. Kirchartz and H. Oertel, Three-dimensional cellular convection in rectangular boxes, *J. Fluid Mech.* **192,** 249–286 (1988).
9. D. Mukutmoni and K. T. Yang, Flow transitions in a three-dimensional rectangular enclosure heated from below, *Proc. ASME/JSME Thermal Engng Conf.*, Reno, Nevada, Vol. 1, pp. 77–82 (1991).
10. D. Mukutmoni and K. T. Yang, Transition to oscillatory flow in Rayleigh–Benard convection in a three-dimensional box. Presented at the ASME National Heat Transfer Conference, Minneapolis, Minnesota (1991).
11. G. D. Mallinson and G. de Vahl Davis, Three-dimensional natural convection in a box: a numerical study, *J. Fluid Mech.* **83,** 1–31 (1977).
12. R. Viskanta, D. M. Kim and C. Gau, Three-dimensional numerical natural convection heat transfer of a liquid metal in a cavity, *Int. J. Heat Mass Transfer* **29,** 475–485 (1986).
13. A. M. Lankhorst and C. J. Hoogendoorn, Three-dimensional calculations of high Rayleigh number natural convection flows in enclosed cavities, *Proc. Natn. Heat Transfer Conf.*, Houston, Texas, Vol. 3, pp. 463–470 (1988).
14. T. Fusegi, J. M. Hyun, K. Kuwahara and B. Farouk, Transient 3-D natural convection in a differentially heated cubical enclosure, *Proc. ASME/JSME Thermal Engng Conf.*, Reno, Nevada, Vol. 1, pp. 83–88 (1991).
15. T. Fusegi, J. M. Hyun, K. Kuwahara and B. Farouk, A numerical study of 3-D natural convection in a differentially heated cubical enclosure, *Int. J. Heat Mass Transfer* **34,** 1543–1557 (1991).
16. H. Ozoe, K. Yamamoto, H. Sayama and S. W. Church-

ill, Natural convection patterns in a long inclined rectangular box heated from below, *Int. J. Heat Mass Transfer* **20,** 131–139 (1977).
17. S. J. M. Linthorst and C. J. Hoogendoorn, Natural convective heat transfer in three dimensional inclined small aspect ratio enclosures, *Proc. 8th Int. Heat Transfer Conf.*, San Francisco, California, pp. 1501–1506 (1986).
18. H. Q. Yang, K. T. Yang and J. R. Lloyd, Flow transition in laminar buoyant flow in a three-dimensional tilted rectangular enclosure, *Proc. 8th Int. Heat Transfer Conf.*, San Francisco, California, pp. 1495–1500 (1986).
19. D. Kuhn and P. H. Oosthuizen, Three-dimensional natural convective flow in a rectangular enclosure with localized heating, *Proc. AIAA Thermophysics Conf.*, pp. 55–62 (1987).
20. K. V. Liu, K. T. Yang and M. D. Kelleher, Three-dimensional natural convection cooling of an array of heated protrusions in an enclosure filled with a dielectric fluid, *Proc. Int. Symp. on Cooling Technology for Electronic Equipment*, Honolulu, Hawaii, pp. 486–497 (1987).
21. K. V. Liu, K. T. Yang, Y. W. Wu and M. D. Kelleher, Local oscillatory surface temperature responses in immersion cooling of a chip array by natural convection in an enclosure, *Proc. Symp. on Heat and Mass Transfer in Honor of B. T. Chao*, University of Illinois, Urbana–Champaign, Illinois (1987).
22. A. M. C. Chan and S. Banerjee, Three-dimensional numerical analysis of transient natural convection in rectangular enclosures, *J. Heat Transfer* **101,** 114–119 (1979).
23. Y. Joshi and R. A. Paje, Natural convection cooling of a ceramic substrate mounted leadless chip carrier in dielectric liquids, *Int. Commun. Heat Mass Transfer* **18,** 39–47 (1991).
24. Product Manual, Flourinert Liquids, 3M Corporation, Minneapolis, Minnesota (1985).
25. S. V. Patankar, *Numerical Heat Transfer and Fluid Flow*, Hemisphere, McGraw-Hill, New York (1980).
26. J. L. Lage and A. Bejan, The *Ra–Pr* domain of laminar natural convection in an enclosure heated from the side, *Numer. Heat Transfer, Part a* **19,** 21–41 (1991).